

Towards Quantitative Reaction Dynamics of O₃

Raidel Martin Barrios, Abhirami Vijayakumar, Jingchun Wang and Markus
Meuwly*

*Department of Chemistry, University of Basel, Klingelbergstrasse 80, CH-4056 Basel,
Switzerland.*

E-mail: m.meuwly@unibas.ch

Abstract

The reaction dynamics of $\text{O}(^3\text{P}) + \text{O}_2(^3\Sigma_g^-)$ collisions in the $\text{O}_3(^1A')$ electronic ground state is characterized on a high-level MRCI+Q/aug-cc-pVQZ potential energy surface represented as a reproducing kernel. For the atom exchange reactions involving the ^{16}O and ^{18}O isotopes as the atomic collision partner, associated with rates $k_6(T)$ and $k_8(T)$, respectively, a negative temperature-dependence of $k(T)$, consistent with experiments was found. The absolute rates typically underestimate measured rates by $\sim 50\%$, depending on the experiment considered. For the ratio $R(T) = k_8(T)/k_6(T)$, the measured T -dependence was found, including a cusp at lower temperatures. The differences between experiments and computations are primarily due to neglect of quantum effects, primarily zero-point effects. For the atomization reaction, leading to $3\text{O}(^3\text{P})$, the rates is lower by approximately one order of magnitude compared with experiments, which is a clear improvement over simulations using previous potential energy surfaces computed with smaller basis sets. Nonadiabatic effects are deemed minor for the atom exchange reactions.

Introduction

Quantitative simulations for small to medium-sized molecules have come into reach over the past few years. One of the deciding factors was to introduce machine learning-based techniques for representing full-dimensional potential energy surfaces (PESs). Another driver was the possibility to carry out electronic structure calculations at sufficiently high levels of theory. Increasingly accurate simulations are not only of interest when comparing measurements with observables from computations. Quantitative gas phase reaction dynamics also provides information about the validity of classical versus quantum treatments of the nuclear dynamics, the relevance of including particular quantum effects, the required level of electronic structure theory for particular observables, or the accuracy with which ML-based

representations need to reproduce the underlying reference calculations.

The reaction dynamics of the $O(^3P) + O_2(^3\Sigma_g^-)$ system is of considerable interest in atmospheric chemistry and in rarefied gas flow.¹⁻⁶ This regime is encountered at the high altitudes relevant to hypersonic flight.⁷⁻⁹ From a chemical perspective, the processes occurring in hypersonic flight can be viewed as a complement to ordinary burning whereby both lead to chemical transformation of the starting material. While "burning" is exothermic and releases chemical energy through fuel oxidation, hypersonic vehicles experience intense aerodynamic heating due to strong mechanical compression (shock waves with local $T \sim 10000$ K or higher), which converts kinetic energy into internal energy. The resulting high post-shock temperatures can dissociate atmospheric N_2 and O_2 , triggering high-temperature air chemistry to generate specifically nitric oxide (NO) via the thermal (Zel'dovich) mechanism,¹⁰⁻¹³ involving reactions between dissociated nitrogen and oxygen species.

In the wider context of the Zel'dovich (thermal NO production) mechanism, the $O+O_2$ chemistry matters mainly because it controls the availability of atomic oxygen, which is the key reactant in the rate-limiting step $N_2+O \leftrightarrow NO+O$, followed by the fast propagation step $O_2+N \rightleftharpoons NO+O$. In hot air (e.g., shock-heated or post-flame gases), NO formation is therefore highly sensitive to the local O-atom pool. Any pathway that converts O into more stable oxygen species reduces the driving reactant for the N_2+O reaction and can suppress generation of thermal NO. On the other hand, O-generating pathways can sustain formation of thermal NO.

In cooler or lower-temperature oxygen-rich regions (more typical of upper-atmosphere/vacuum and some rarefied near-wall zones than of the hottest shock layer), the relevant O_2+O sink is often the termolecular association $O_2+O+M \rightarrow O_3+M$ reaction, which is collision-limited and can act as an O-atom reservoir/sink that indirectly modulates the Zel'dovich chain

through changing [O] concentration. Importantly, the entire chemistry in hypersonic flight is shock-induced and evolves under extreme non-equilibrium conditions, with populations far from equilibrium with respect to occupation of translational, rotational, vibrational, and electronic degrees of freedom.

A particular motivation for the present work is provided by the observation that recent quasi-classical trajectory (QCT) simulations on good-quality PESs underestimated measured dissociation rates for the $\text{O}(^3\text{P}) + \text{O}_2(^3\Sigma_g^-)$ by two orders of magnitude. One of the debated ingredients for treating such processes is the electronic degeneracy for which different values (ranging from 1/27 to 16/3) have been proposed in the literature. With a higher-level treatment it should be possible to considerably narrow down this interval. Another reason to consider the $\text{O}(^3\text{P}) + \text{O}_2(^3\Sigma_g^-)$ reaction system is the fact that two rather different PESs yielded comparable $k(T)$ for the atom exchange and dissociation reactions. This indicates that consistency with experiments is not coincidental and improving one of the two provides additional insights.

The present work also considers isotopic effects on the atom exchange reaction.¹⁴ This aspect is of particular relevance in the wider context of isotopic fractionation in ozone with particular emphasis on atmospheric chemistry.¹⁵ Ozone formation produces a distinctive mass-independent fractionation (MIF) in oxygen isotopes (an anomalous $\Delta^{17}\text{O}$ signal) that cannot be explained by ordinary mass-dependent kinetics. Hence, the MIF an important diagnostic of ozone chemistry and its coupling to broader oxidant cycles. This “ozone anomaly” was first demonstrated in laboratory ozone production and established that chemical reactions can generate large, non-mass-dependent isotope effects in oxygen, fundamentally changing how atmospheric isotope signals are interpreted.¹⁵ Building on this, mechanistic work showed that the anomaly is rooted in molecular-level dynamics of the ozone-forming recombination reaction. Hence, ozone isotopologues provide a sensitive probe of formation/stabilization

pathways under different conditions.¹⁶ Crucially, ozone’s $\Delta^{17}\text{O}$ signature propagates into secondary atmospheric products through ozone-involving oxidation (e.g., pathways leading to nitrate).

The present work is structured as follows. First, the methods are presented, followed by the validation of the PES. Next, the results from QCT simulations for the atom exchange and atomization reactions are discussed. Finally, conclusions are drawn.

Methods

Reactive potential energy surface

The ground-state reactive PES of the system $\text{O}_3(^1A')$ was constructed using high-level *ab initio* electronic structure calculations combined with a reproducing kernel Hilbert space (RKHS) representation. All reference energies were computed at the multireference configuration interaction level including the Davidson correction (MRCI+Q),^{17,18} employing the augmented correlation-consistent polarized quadruple-zeta basis set (aug-cc-pVQZ, AVQZ).¹⁹

Electronic structure calculations were carried out using Jacobi coordinates, where R denotes the distance between the incoming atom and the center of mass of the diatomic fragment, r is the diatomic bond length, and θ is the angle between the vectors \mathbf{R} and \mathbf{r} . Calculations were performed assuming C_S symmetry using the MOLPRO suite of programs.²⁰ The reference data set was generated on a three-dimensional grid spanning the physically relevant regions of configuration space, including both bound and near-dissociation geometries. The grid comprising $R \in [1.4, 13.0] a_0$, $r \in [1.1, 4.16] a_0$, and $\theta \in [90.1^\circ, 169.8^\circ]$ following the same methodology of previous work.²¹ The spacing was non-uniform and refined in the interaction region, with denser sampling at short intermolecular separations and near the equilibrium

bond length of the diatomic fragment. This results in a total of 2550 geometrically distinct and physically meaningful ground-state configurations.

To properly describe the electronic structure along the reactive coordinates, state-averaged complete active space self-consistent field CASSCF(12,9) calculations were first carried out and used as reference wave functions for the subsequent MRCI+Q computations. The MRCI+Q approach was adopted instead of conventional MRCI in order to improve the overall accuracy of the electronic structure calculations, as the inclusion of the Davidson correction significantly reduces the size-consistency error inherent to standard MRCI.^{22,23} Multiple electronic states were included in the state-averaging procedure to ensure smooth behavior of the PES across different regions of configuration space. In cases where convergence issues were encountered or where reference points were missing, the data set was completed using lower-dimensional RKHS interpolations prior to constructing the full three-dimensional surface. The final three-dimensional RKHS representation was generated using the KERNEL-TOOLKIT.²⁴

The global reactive PES was constructed by combining three single-channel PESs corresponding to the three possible atom-diatom arrangements using a permutationally invariant mixing scheme. The total potential was written as

$$V(\vec{r}) = \sum_{i=1}^3 w_i(r_i) V_i(\vec{r}), \quad (1)$$

where $\vec{r} = (r_{AB}, r_{AC}, r_{BC})$ denotes the set of interatomic distances. The channel weights w_i were defined using an exponential switching function,

$$w_i(r_i) = \frac{\exp[-(r_i/\rho)^2]}{\sum_{j=1}^3 \exp[-(r_j/\rho)^2]}, \quad (2)$$

with a single optimized switching parameter ρ . The value of $\rho = 1.63 a_0$ was determined

through a grid-based optimization using an independent mixing data set specifically designed to sample the regions where multiple channels overlap. The mixing data set was constructed on a grid defined by angular configurations $\theta = 30^\circ, 60^\circ, 90^\circ, 120^\circ, 150^\circ$, while the interatomic distances r_{AB} and r_{BC} were sampled identically in the range 2.30–4.00, a_0 , using a non-uniform spacing refined in the channel crossing region.

The quality of the PES was assessed by evaluating the root-mean-square deviation (RMSD) and correlation coefficient r^2 for on-grid, mixing, and off-grid validation data sets. The off-grid validation geometries were generated using angular values $\theta = 20^\circ, 40^\circ, 80^\circ, 130^\circ, 160^\circ$, with both interatomic distances r_{AB} and r_{BC} spanning the interval 1.9–5.1, a_0 . These configurations were excluded from both the construction of the single-channel PESs and the optimization of the mixing parameters in the channel-crossing regions. The resulting PES accurately reproduces the reference MRCI+Q/AVQZ energies over a wide energy range, including configurations well above the dissociation limit.

Quasi-classical trajectory simulations

Quasi-classical trajectory simulations were performed on the constructed RKHS-PES to investigate the reaction dynamics and compute thermal rate coefficients. Initial conditions were sampled semiclassically from Boltzmann distributions of translational energy E_{trans} , impact parameter b , total angular momentum J , and rovibrational states (v, j) of the diatomic molecule. To ensure statistical convergence, 5×10^6 independent quasi-classical trajectory simulations were performed at each temperature. The trajectories were propagated until any interatomic distance exceeded a cutoff of $20 a_0$, indicating that the fragments were fully separated (atomization), or until the maximum simulation time of 75 ps was reached. The reaction outcomes were then identified using geometrical criteria based on the interatomic distances. Atom exchange was assigned when one pair of atoms formed a diatom ($r_{ij} < 8 a_0$)

while the other two interatomic distances exceeded $16 a_0$, indicating the formation of a new diatomic bond and the separation of the third atom.

Thermal rate coefficients at a given temperature T were computed according to

$$k(T) = g_e(T) \sqrt{\frac{8k_B T}{\pi \mu}} \pi b_{\max}^2 \frac{N_r}{N_{\text{tot}}}, \quad (3)$$

where μ is the reduced mass, b_{\max} is the maximum impact parameter, N_r is the number of reactive trajectories, and N_{tot} is the total number of trajectories, and k_B is the Boltzmann constant. The factor $g_e(T)$ accounts for the electronic degeneracy of the reaction channel under consideration. For the atom exchange process, the temperature-dependent electronic degeneracy factor was²⁵⁻²⁷

$$g_e^{\text{exch}}(T) = 1/\{3 [5 + 3 \exp(-277.6/T) + \exp(-325.9/T)]\}. \quad (4)$$

In contrast, for the full dissociation reaction and in the absence of nonadiabatic effects, a temperature-independent electronic degeneracy of $g_e^{\text{diss}} = 1/27$ was used here, also following earlier work.²⁵ It is worth noting that alternative temperature-independent electronic degeneracy factors have been adopted in previous studies, most notably a value of $g_e^{\text{diss}} = 16/3$. This choice, however, was originally introduced for the Ar + O₂ dissociation system and later transferred to the present context. The two values $g_e^{\text{diss}} = 16/3$ and $g_e^{\text{diss}} = 1/27$ should therefore be regarded as approximate upper and lower limits, respectively. As a consequence, the dissociation rate $k_{\text{diss}}(T)$ reported in this work, which is based on $g_e^{\text{diss}} = 1/27$, represents a lower bound to the corresponding temperature-dependent rate. Statistical uncertainties were estimated using bootstrap resampling.²⁸ For each temperature, the full trajectory set was divided into multiple batches, and random resampling was used to obtain standard deviations for the computed rates.

Results

Validation of the AVQZ-RKHS-PES

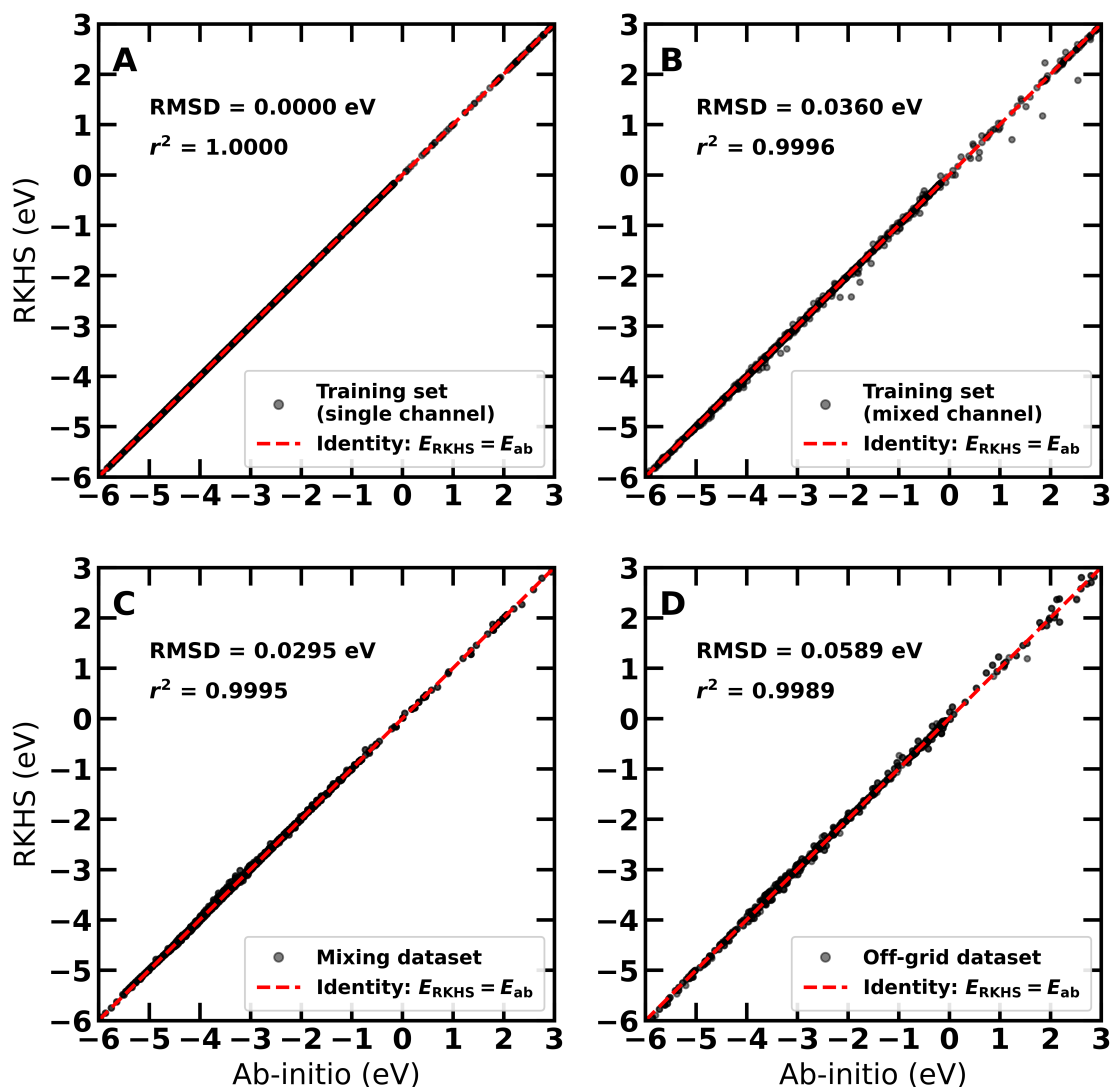


Figure 1: Performance of the RKHS-represented reactive, three-dimensional PES for the [OOO] system with the zero of energy at the $\text{O}(^3\text{P})+\text{O}(^3\text{P})+\text{O}(^3\text{P})$ asymptote. (A) Correlation between single-channel RKHS representation and reference energies for on-grid training data. (B) Correlation between 3D mixed RKHS representation and reference energies for the on-grid training data. (C) Performance of the 3D mixed RKHS representation on the mixing region. (D) Performance of the 3D mixed RKHS representation for 1188 off-grid points not used in constructing the PES. The RMSD between the RKHS representation and the reference data and the corresponding r^2 are given in each panel.

Figure 1 reports statistical performances of the non-reactive and reactive potential energy

surfaces. The single-channel PES (Figure 1A) featured a representation error of $\text{RMSD} < 10^{-5}$ eV (0.0002 kcal/mol) and $r^2 = 1.0$ across 9 eV. Such a performance is on par with previous work.^{21,29} Panel B reports the performance of the mixed surface, see Eq. 2, on the reference data set. The $\text{RMSD}(E)$ increases to 0.0360 eV with $R^2 = 0.9996$. In order to further refine the mixed PES around the crossing regions, the mixing parameter was refined by fitting to the mixing data set which features an $\text{RMSD}(E)$ of 0.0295 eV and associated $R^2 = 0.9995$, see Figure 1C.

Finally, the performance of the mixed, 3-channel PES was assessed on a test set in which all geometries are “off-grid” with respect to all available configurations used to construct the single- and 3-channel PESs. Figure 1D underscores the high quality of the reactive PES for the [OOO] system with $\text{RMSD}(E) = 0.0589$ eV (1.35 kcal/mol) across an energy range of 9 eV (210 kcal/mol). Evidently, the performance is considerably better for energies below the $\text{O}(^3\text{P})+\text{O}(^3\text{P})+\text{O}(^3\text{P})$ asymptote. As a comparison, the performance of a recent PIP-based PES across 200 kcal/mol was $\text{RMSD}(E) \sim 4.5$ kcal/mol.³⁰

Next, the overall shapes of the AVTZ- and AVQZ-RKHS potential energy surfaces was compared. The AVTZ-RKHS surface was previously validated from comprehensive QCT simulations vis-a-vis thermal rates $k(T)$ for the T -dependence of the atom-exchange and the atomization reaction.²¹ Figure 2 reports the shapes $V(R, \theta)$ of the two PESs for given O–O separation. As Figure 2A shows, the isocontours for the two PESs closely follow each other and the total interaction energy using the AVQZ basis set is consistently lower than for the AVTZ basis set. As an example, the stabilization of the O_3 structure ($R = 3.14 a_0, \theta = 43.6^\circ$) between the AVTZ- and AVQZ-RKHS PESs increases from -26.4 kcal/mol to -29.6 kcal/mol. This indicates that for given collision energy the thermal rates on the higher-level AVQZ-PES are expected to decrease compared with those from QCT simulation using the AVTZ-PES.

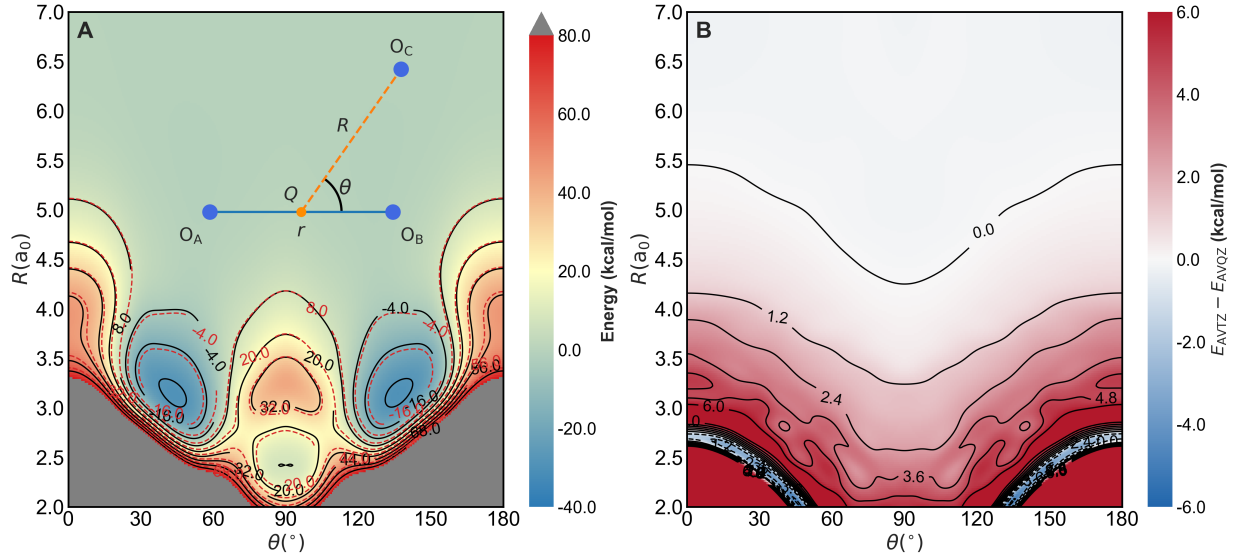


Figure 2: Panel A: Two-dimensional potential energy surface (PES) for a fixed internuclear distance $r = 2.46$ a.u. as a function of the Jacobi coordinates (R, θ) , computed at the AVQZ level. The color scale represents the energy in kcal/mol. Solid black contour lines correspond to AVQZ energies, while dashed red contours indicate AVTZ results for comparison. The inset illustrates the definition of the Jacobi coordinates: r is the diatomic bond length between O_A and O_B , R is the distance from the diatomic center of mass Q to atom O_C , and θ is the angle between \vec{r} and \vec{R} . Panel B: Energy difference surface $E_{AVTZ} - E_{AVQZ}$ as a function of (R, θ) . The color map highlights regions where AVTZ overestimates (red) or underestimates (blue) the AVQZ energies. Contour lines are drawn at uniform intervals. The minimum energy in the reactant well region is found to be $E_{AVQZ}^{\min} = -29.6$ kcal/mol and $E_{AVTZ}^{\min} = -26.4$ kcal/mol within the selected (R, θ) window.

The Atom Exchange and Isotopic Substitution Reactions

First, QCT simulations using the AVQZ-PES were carried out to characterize the atom-exchange reaction for the natural and the heavy isotope of the incoming oxygen atom. This reaction is characterized by the exchange of the incoming oxygen atom O_A by one of the oxygen atoms O_B or O_C forming the O_2 molecules: $O_A + O_B O_C \rightarrow O_B + O_A O_C$ or $\rightarrow O_C + O_A O_B$. In addition to $^{16}O_A + ^{16}O_B ^{16}O_C$, simulations were also carried out for isotopic variants to determine the rates $k_6(T)$ and $k_8(T)$, respectively.¹⁴ Here, $k_6(T)$ and $k_8(T)$ refer to the ^{16}O and ^{18}O isotopes as the collision partner of $^{18}O^{18}O$ and $^{16}O^{16}O$, respectively.

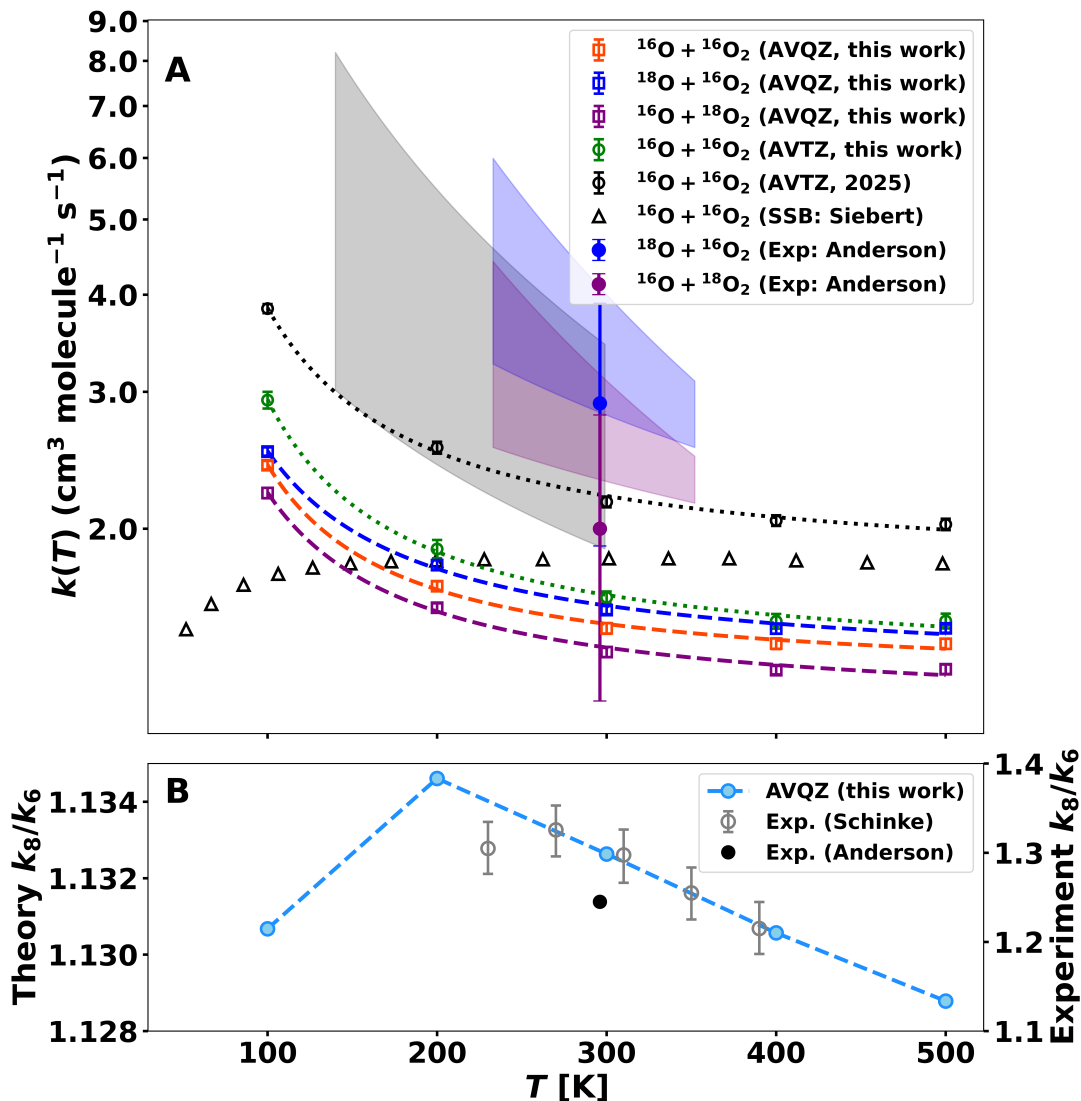


Figure 3: Temperature dependence of the thermal rate coefficients $k(T)$ for the natural and heavy isotope of the incoming oxygen atom. Panel A: Results for $k(T)$ obtained from the RKHS-based PESs using the AVTZ and AVQZ basis sets and for oxygen isotopic substitutions as indicated in the legend. Earlier wave packet simulations using the SSB PES (black triangles) illustrate the negative T -dependence a number of previous studies reported.³¹ The measured rates³² (blue and violet filled circles) are shown together with the reported uncertainties. Other measured rates are represented by the shaded uncertainty regions: blue and violet¹⁴ for $^{18}\text{O} + ^{16}\text{O}_2$ and $^{16}\text{O} + ^{18}\text{O}_2$, respectively, while the gray³³ region applies to both. Panel B: T -dependence of the isotopic rate ratio $R(T) = k_8(T)/k_6(T)$. Theoretical predictions obtained with the AVQZ RKHS-PES (blue symbols) are compared with measurements^{14,32} (grey and black symbols).

Using the new AVQZ-RKHS PES for the $^{16}\text{O} + ^{16}\text{O}^{16}\text{O}$ exchange reaction (orange), the expected negative T -dependence was found. In verifying the previous results using the

AVTZ-RKHS PES it was realized that an erroneous reduced mass was employed in the earlier study.²¹ The previous (black) and corrected (green) exchange rates using the AVTZ-RKHS PES are also reported in Figure 3A. The T -dependence remains unchanged but $k(T)$ decreases by $\sim 25\%$ using the correct reduced mass. Finally, results for the systems for which measurements have been carried out - $^{18}\text{O} + ^{16}\text{O}^{16}\text{O}$ (blue) and $^{16}\text{O} + ^{18}\text{O}^{18}\text{O}$ (violet) - are also shown in Figure 3B. With increasing mass of the collision system the thermal rates decrease by a few percent. This is consistent with two earlier experimental studies^{14,32} but at variance with a third one.³³ When comparing absolute values for $k(T)$ it should be noted that the QCT simulations do not include zero point vibrational energy which has been identified as an ingredient required for quantitative comparisons between simulations and experiment.¹⁴

The shaded black and colored regions in Figure 3A, show the reported experimental uncertainty ranges from the literature data.^{33,34} and values at 296 K from another experimental study.³² The T -dependent experiments feature $k(T)$ that decreases with increasing temperature. This observation and the fact that several simulation studies reported a positive T -dependence has lead to intense discussions regarding the overall shape of the PES. Specifically, a so-called "reef" along the minimum energy path for the atomic oxygen approaching the O_2 collision partner at long range had been proposed to lead to the disagreement between measurements and simulations.^{14,35-39} Recently, however, it has been established²¹ from QCT simulations using two different high-level reactive and global PESs (at MRCI+Q²¹ and CASPT2³⁰ levels) for the [OOO] collision system that the "reef" is an integral feature of the PESs and not an artifact and leads to the T -dependence consistent with experiments. Furthermore, the "reef" has been known for some time from electronic structure calculations at different levels of theory.⁴⁰⁻⁴²

Figure 3B reports the T -dependence of the isotopic rate ratio $R(T) = k_8(T)/k_6(T)$, which

provides another sensitive probe of the PESs and the underlying dynamics. The ratio $R(T)$ has also been measured and found to have a cusp-like structure with a maximum around 300 K (grey symbols in panel B).¹⁴ The present simulations feature this cusp and the slope towards higher temperatures but the magnitude is too low compared with the experiments. Another experiment reported $R(T = 296\text{K}) = 1.245$, which is also indicated in the Figure (black).³² As already mentioned, including zero point energy differentially influences the values of $k_6(T)$ and $k_8(T)$ and therefore affects $R(T)$ as well. However, the overall behaviour of $R(T)$ is not expected to change dramatically.

The Atomization Reaction

Next, the atomization reaction $\text{O}(^3\text{P}) + \text{O}_2(^3\Sigma_g^-) \rightarrow 3\text{O}(^3\text{P})$ was considered. For this process, measurements to compare with are also available.^{43,44} The QCT results using the AVQZ-PES (dark red) correctly capture the T -dependence of the measured rates (open circles and dashed lines). Using $g_e^{\text{diss}} = 1/27$ the absolute magnitude of the measured rates is underestimated by \sim one order of magnitude. This compares with a difference of \sim two orders of magnitude from simulations using triple-zeta-quality PESs (red and blue symbols) from previous work,²¹ which also employed $g_e^{\text{diss}} = 1/27$. Hence, the higher-level PES clearly improves the agreement with experiment but still underestimates the magnitude of the dissociation rate.

The improvement demonstrates the sensitivity of the dissociation dynamics to the quantitative accuracy of the underlying potential energy surface. The use of the larger aug-cc-pVQZ (AVQZ) basis set provides a more complete treatment of electron correlation and a more accurate representation of the interaction energies, which directly impacts on the O_2 dissociation energy, as already reported previously.²¹ Consequently, the AVQZ-based PES yields rate coefficients that are in substantially better agreement with the experimental data^{43,44}

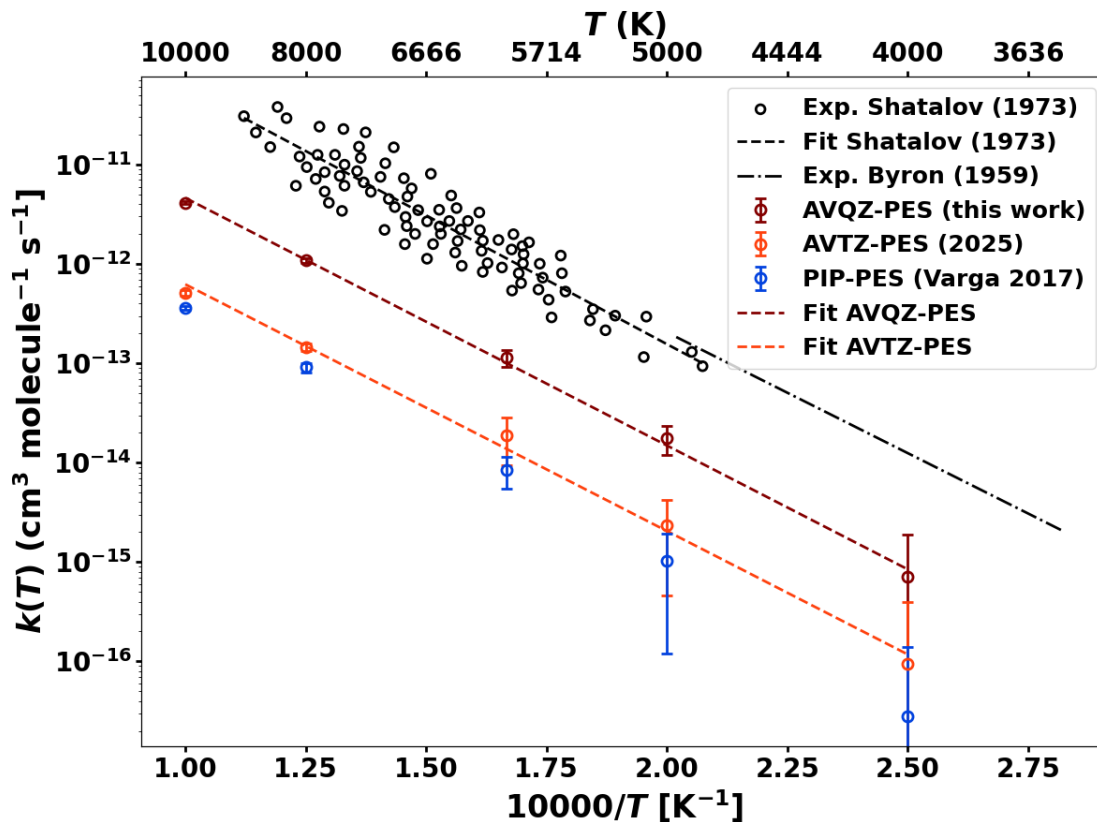


Figure 4: Thermal rate coefficients $k(T)$ for the dissociation reaction using $g_{\text{diss}} = 1/27$. The rate constants are shown as a function of inverse temperature ($10000/T$) on the lower horizontal axis, while the corresponding temperature scale (in K) is displayed on the upper axis. Simulation results obtained with different potential energy surfaces are shown as colored symbols, including statistical error bars estimated via bootstrapping. Results based on the RKHS-PES constructed with the AVTZ²¹ and AVQZ (present work) basis sets are shown as red open circles and dark red symbols, respectively, while those using the PIP-PES^{21,30} are the blue symbols. To visually emphasize the temperature dependence, the AVTZ and AVQZ simulation results were fitted and are represented by dashed lines in their respective colors. Experimental measurements^{43,44} are shown as black open circles. A linear regression of the experimental data is indicated by the dashed black line.

than those obtained with the AVTZ-based surface. This emphasizes the importance of basis-set convergence for achieving quantitatively reliable reaction dynamics simulations.

Discussion and Conclusions

The present work reports thermal rates for the atom exchange and dissociation reactions for the $\text{O}(^3\text{P}) + \text{O}_2(^3\Sigma_g^-)$ system using a high-level MRCI+Q/AVQZ PES represented as a RKHS. For the atom exchange reaction the T -dependence is consistent with the measurements whereas the magnitude of the rates is lower by a factor of ~ 2 . For the dissociation reaction the T -dependence of the experiments is correctly captured whereas the magnitude of the rate is lower by about one order of magnitude. Notably, the ratio $R(T) = k_8(T)/k_6(T)$ which compares the rates for the $^{18}\text{O} + ^{16}\text{O}_2$ exchange reaction with that for $^{16}\text{O} + ^{18}\text{O}_2$ mirrors that reported from measurements:¹⁴ starting from low- T , $R(T)$ increases, reaches a cusp and then decreases monotonically towards higher T . However, the temperature at which the cusp appears is lower by several 10 K and the magnitude of $R(T)$ is clearly underestimated.

It is also of interest to consider the possible role of crossings between the singlet PESs. For this, the energies of the lowest 4 excited singlet states ($2^1\text{A}'$ to $5^1\text{A}'$) were evaluated on the same grid as the $1^1\text{A}'$ ground state. Up to this point, the energies of the excited states were not represented as a RKHS. This is outside the main scope of the present work but will follow similar lines of previous work on the $\text{C}+\text{O}_2$ reaction.⁴⁵ It has already been reported that non-adiabatic effects are unlikely to be the reason for disagreements between simulations and measurements for the atom-exchange reaction.^{34,46} In order to assess whether using the larger AVQZ basis set leads to the same conclusion, part of the relevant potential energy surfaces are considered in Figure 5.

One-dimensional cuts for $r_{\text{OO}} = 2.65 a_0$ and three angles θ are considered. Here, the zero of energy is the minimum of the ground-state $1^1\text{A}'$ surface (Figure 5B, blue symbols). For structures around the minimum ($\theta = 156.6^\circ$ and $\theta = 129.9^\circ$; panels A and B) no crossings between the ground and the excited state PESs are found. However, distortion to $\theta = 90^\circ$ (panel C) leads to a crossing of the $2^1\text{A}'$ and $3^1\text{A}'$ states with the $1^1\text{A}'$ ground state at

$R = 3.36 a_0$. Hence, in this region the exchange reaction $O(^3P) + O_2(^3\Sigma_g^-)$ asymptotically may lead to excited state products $O^1D + O_2(a^1\Delta_g)$ if the trajectory follows the diabatic PES. The shapes and relative energetics of the excited state surfaces are consistent with earlier work.⁴⁷

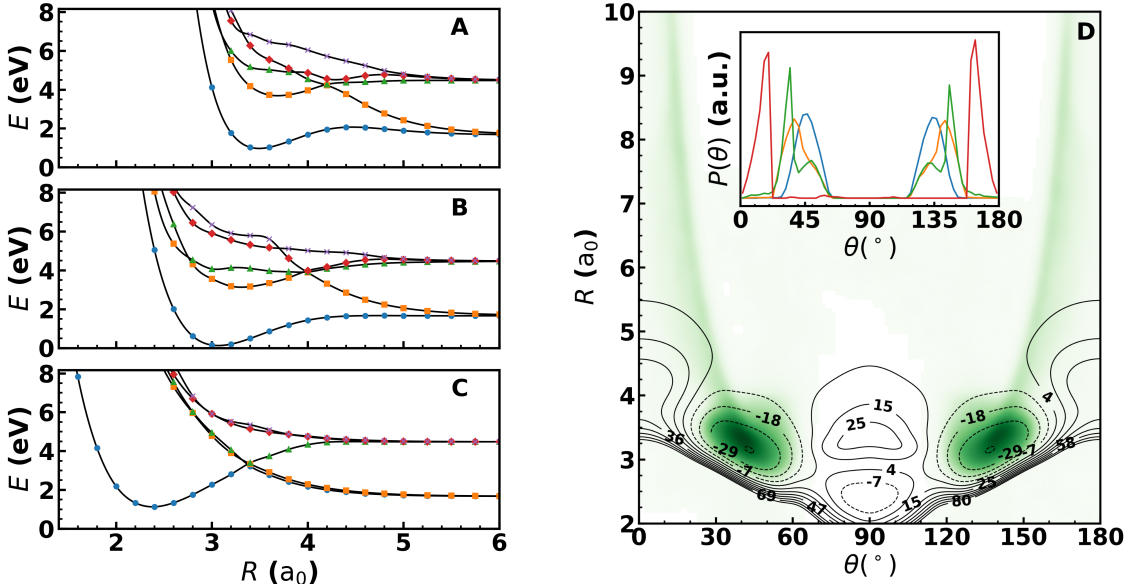


Figure 5: Potential energy curves of the five lowest $^1A'$ electronic states ($1^1A'$ (blue), $2^1A'$ (orange), $3^1A'$ (green), $4^1A'$ (red), and $5^1A'$ (purple)) as functions of the dissociation coordinate R for fixed angles $\theta = 156.6^\circ$, $\theta = 129.9^\circ$ and $\theta = 90.1^\circ$ (panels A to C). The O–O bond distance was $r = 2.65 a_0$. The zero of energy is the minimum of the ground-state surface (panel B). In A to C, colored symbols denote adiabatic *ab initio* MRCI energies, while solid black lines represent the corresponding diabatic potential energy curves. Panel D: Projection of the distribution $P(R, \theta)$ (green) from 1500 trajectories run at 100 K, leading to atom exchange onto the adiabatic ground-state potential energy surface $V(R, \theta; r = 2.65 a_0)$. Inset: Angular distribution $P(\theta)$ for $R = 3.0 a_0$ (blue), $R = 3.5 a_0$ (orange), $R = 4.0 a_0$ (green), and $R = 7 a_0$ (red). Note the near-symmetry of $P(\theta)$ with respect to $\theta = 90^\circ$.

Figure 5D illustrates the probability distribution $P(R, \theta)$ of trajectories run at 100 K on the $1^1A'$ PES and leading to atom exchange on their way to products, projected onto the adiabatic ground state PES $V(R, \theta; r = 2.65 a_0)$. For regions in (R, θ) –space for which crossings between the $1^1A'$ and the $2^1A'$ / $3^1A'$ surfaces occur, the trajectories can potentially change electronic states due to strong coupling. Instead of the ground state products $O(^3P)$

+ $\text{O}_2(^3\Sigma_g^-)$ after atom exchange, electronically excited products will be formed. Such processes will reduce the rate for the particular process considered, which is “atom exchange” in the present case. However, the (R, θ) -configurations sampled after atom exchange has taken place demonstrates that the region in which the $1^1\text{A}'$ and the $2^1\text{A}' / 3^1\text{A}'$ PES cross ($\theta \sim 90^\circ$) is not visited. This is most clearly seen in the inset in Figure 5D. Hence, the present QCT simulations indicate that nonadiabatic effects play a minor role for the atom exchange reaction at T up to 500 K which is consistent with earlier findings.³⁴

Underestimating $k(T)$ for the exchange reaction is primarily a consequence of neglecting zero-point energy (ZPE) in the QCT simulations.^{14,46} Hence, the present finding is reassuring. Also, the rates from using the RKHS/AVTZ²¹ and RKHS/AVQZ PESs are consistent with one another. Accounting for ZPE will also change $R(T)$. Finally, nonadiabatic processes are unlikely to contribute significantly for the atom exchange reaction because the crossing region between the $1^1\text{A}'$ ground state and the two lowest excited singlet states ($2^1\text{A}' / 3^1\text{A}'$) is not sampled for the trajectories leaving the strongly interacting region after atom exchange has taken place, see Figure 5D.

As to $k(T)$ for the atomization reaction, it is found that the agreement with experiment improves by one order of magnitude compared with simulations based on the RKHS/AVQZ PES, using $g_e = 1/27$ as in previous work^{21,25} excluding nonadiabatic effects. On the other hand, it should be noted that the “correct” electronic degeneracy is not known: T -independent values ranging from $g_e = 16/3$ (borrowed from the $\text{Ar} + \text{O}_2$ dissociation reaction⁴⁸) down to $g_e = 1/27$ have been used in the literature.^{21,25,49–51} Both, the magnitude and assuming a T -independent value for g_e are idealizations.

In conclusion, the RKHS/AVQZ PES represents a clear improvement in QCT simulations for the atomization rate and corroborates the findings of a negative T -dependence for the

atom-exchange reaction. Notably, the shape and T -dependence for $R(T)$ is consistent with experiments. Studies as the one presented here demonstrate that atomistic simulations for chemical reactions have reached a mature state in which reasons for remaining disagreement between results from computations and measurements can be further narrowed-down in order to reach a more profound understanding of the processes in question.

Data Availability

The codes and data for the present study are available from <https://github.com/MMunibas/o3-avqz> upon publication.

Acknowledgment

The authors gratefully acknowledge financial support from the Swiss National Science Foundation through grants 200020_219779 (MM), 200021_215088 (MM), and the University of Basel (MM). This article is also based upon work within COST Action COSY CA21101, supported by COST (European Cooperation in Science and Technology) (to MM).

References

- (1) Koner, D.; Unke, O. T.; Boe, K.; Bemish, R. J.; Meuwly, M. Exhaustive state-to-state cross sections for reactive molecular collisions from importance sampling simulation and a neural network representation. *J. Chem. Phys.* **2019**, *150*, 211101.
- (2) Arnold, J.; San Vicente Veliz, J. C.; Koner, D.; Singh, N.; Bemish, R. J.; Meuwly, M. Machine learning product state distributions from initial reactant states for a reactive atom-diatom collision system. *J. Chem. Phys.* **2022**, *156*, 034301.

- (3) Koner, D.; Bemish, R. J.; Meuwly, M. Dynamics on multiple potential energy surfaces: Quantitative studies of elementary processes relevant to hypersonics. *J. Phys. Chem. A* **2020**, *124*, 6255–6269.
- (4) Park, C. *Nonequilibrium Hypersonic Aerothermodynamics*; Wiley: New York, NY, 1990.
- (5) Park, C. Review of chemical-kinetic problems of future NASA missions. I-Earth entries. *J. Thermophys. Heat Transf.* **1993**, *7*, 385–398.
- (6) Munafò, A.; Liu, Y.; Panesi, M. Development of a two-dimensional binning model for N₂ rovibrational relaxation and dissociation. *J. Chem. Phys.* **2016**, *145*, 064302.
- (7) Sarma, G. Physico-chemical modelling in hypersonic flow simulation. *Progr. Aerospace Sci.* **2000**, *36*, 281–349.
- (8) Knight, D.; Longo, J.; Drikakis, D.; Gaitonde, D.; Lani, A.; Nompelis, I.; Reimann, B.; Walpot, L. Assessment of CFD capability for prediction of hypersonic shock interactions. *Progr. Aerospace Sci.* **2012**, *48-49*, 8–26.
- (9) Boyd, I. D.; Schwartztruber, T. E. *Nonequilibrium Gas Dynamics and Molecular Simulation*; Cambridge University Press, New York, 2017.
- (10) Zel'dovich, Y. B. The oxidation of nitrogen in combustion and explosions. *Doklady Akademii Nauk SSSR* **1946**, *51*, 357–360.
- (11) Bose, D.; Candler, G. V. Thermal rate constants of the N₂+O → NO+N reaction using *ab initio* ³A'' and ³A' potential energy surfaces. *J. Chem. Phys.* **1996**, *104*, 2825–2833.
- (12) Koner, D.; San Vicente Veliz, J. C.; Bemish, R. J.; Meuwly, M. Accurate reproducing kernel-based potential energy surfaces for the triplet ground states of N₂O and dynamics for the N + NO ↔ O + N₂ and N₂ + O → 2N + O reactions. *Phys. Chem. Chem. Phys.* **2020**, *22*, 18488–18498.

- (13) Singh, N.; Schwartzentruber, T. E. Nonequilibrium internal energy distributions during dissociation. *Proc. Natl. Acad. Sci.* **2018**, *115*, 47–52.
- (14) Fleurat-Lessard, P.; Grebenshchikov, S. Y.; Schinke, R.; Janssen, C.; Krankowsky, D. Isotope dependence of the O+ O₂ exchange reaction: Experiment and theory. *J. Chem. Phys.* **2003**, *119*, 4700–4712.
- (15) Thiemens, M. H.; Heidenreich, J. E. The mass-independent fractionation of oxygen: a novel isotope effect and its possible cosmochemical implications. **1983**, *219*, 1073–1075.
- (16) Ivanov, M. V.; Babikov, D. On molecular origin of mass-independent fractionation of oxygen isotopes in the ozone forming recombination reaction. *Proc. Natl. Acad. Sci.* **2013**, *110*, 17708–17713.
- (17) Langhoff, S. R.; Davidson, E. R. Configuration interaction calculations on the nitrogen molecule. *Int. J. Quant. Chem.* **1974**, *8*, 61–72.
- (18) Werner, H.-J.; Knowles, P. J. An efficient internally contracted multiconfiguration–reference configuration interaction method. *J. Chem. Phys.* **1988**, *89*, 5803–5814.
- (19) Dunning Jr, T. H. Gaussian basis sets for use in correlated molecular calculations. I. The atoms boron through neon and hydrogen. *J. Chem. Phys.* **1989**, *90*, 1007–1023.
- (20) Werner, H.; Knowles, P. J.; Manby, F. R.; Black, J. A.; Doll, K.; Heßelmann, A.; Kats, D.; Köhn, A.; Korona, T.; Kreplin, D. A. et al. Molpro, version 2020.1, a package of ab initio programs. *WIREs Comput. Mol. Sci* **2020**, *2*, 242–253.
- (21) Wang, J.; Veliz, J. C. S. V.; Upadhyay, M.; Meuwly, M. High-Energy Reaction Dynamics of O₃. *J. Chem. Phys.* **2025**, *163*, 074109.
- (22) Rintelman, J. M.; Adamovic, I.; Varganov, S.; Gordon, M. S. Multireference second-order perturbation theory: How size consistent is “almost size consistent”. *J. Chem. Phys.* **2005**, *122*, 044105.

- (23) Shiozaki, T.; Knizia, G.; Werner, H.-J. Explicitly correlated multireference configuration interaction: MRCI-F12. *J. Chem. Phys.* **2011**, *134*.
- (24) Unke, O. T.; Meuwly, M. Toolkit for the Construction of Reproducing Kernel-based Representations of Data: Application to Multidimensional Potential Energy Surfaces. *J. Chem. Inf. Model.* **2017**, *57*, 1923–1931.
- (25) Fleurat-Lessard, P.; Grebenshchikov, S. Y.; Siebert, R.; Schinke, R.; Halberstadt, N. Theoretical investigation of the temperature dependence of the O + O₂ exchange reaction. *J. Chem. Phys.* **2003**, *118*, 610–621.
- (26) Jiang, B.; Guo, H. Relative efficacy of vibrational vs. translational excitation in promoting atom-diatom reactivity: Rigorous examination of Polanyi’s rules and proposition of sudden vector projection (SVP) model. *J. Chem. Phys.* **2013**, *138*, 234104.
- (27) Gross, A.; Billing, G. D. Isotope effects on the rate constants for the processes O₂ + O → O + O₂ and O₂ + O + Ar → O₃ + Ar on a modified ground-state potential energy surface for ozone. *Chem. Phys.* **1997**, *217*, 1–18.
- (28) Mooney, C. Z.; Duval, R. D. *Bootstrapping: A Nonparametric Approach to Statistical Inference*; Sage University Paper series on Quantitative Applications in the Social Sciences; SAGE Publications: Newbury Park, CA, 1993.
- (29) Wang, J.; San Vicente Veliz, J. C.; Meuwly, M. High-Energy Reaction Dynamics of N₃. *J. Phys. Chem. A* **2024**, *128*, 8322–8332.
- (30) Varga, Z.; Paukku, Y.; Truhlar, D. G. Potential energy surfaces for O + O₂ collisions. *J. Chem. Phys.* **2017**, *147*, 154312.
- (31) Siebert, R.; Schinke, R.; Bittererová, M. Spectroscopy of ozone at the dissociation threshold: Quantum calculations of bound and resonance states on a new global potential energy surface. *Phys. Chem. Chem. Phys.* **2001**, *3*, 1795–1798.

- (32) Anderson, S. M.; Hülsebusch, D.; Mauersberger, K. Surprising rate coefficients for four isotopic variants of $O + O_2 + M$. *J. Chem. Phys.* **1997**, *107*, 5385–5392.
- (33) Wiegell, M. R.; Larsen, N. W.; Pedersen, T.; Egsgaard, H. The temperature dependence of the exchange reaction between oxygen atoms and dioxygen molecules studied by means of isotopes and spectroscopy. *Int. J. Chem. Kinet.* **1997**, *29*, 745–753.
- (34) Tashiro, M.; Schinke, R. The effect of spin–orbit coupling in complex forming $O(^3P) + O_2$ collisions. *J. Chem. Phys.* **2003**, *119*, 10186–10193.
- (35) Babikov, D.; Kendrick, B. K.; Walker, R. B.; T Pack, R.; Fleurat-Lesard, P.; Schinke, R. Metastable states of ozone calculated on an accurate potential energy surface. *J. Chem. Phys.* **2003**, *118*, 6298–6308.
- (36) Ayouz, M.; Babikov, D. Global permutationally invariant potential energy surface for ozone forming reaction. *J. Chem. Phys.* **2013**, *138*, 164311.
- (37) Dawes, R.; Lolur, P.; Li, A.; Jiang, B.; Guo, H. Communication: An accurate global potential energy surface for the ground electronic state of ozone. *J. Chem. Phys.* **2013**, *139*, 201103.
- (38) Li, Y.; Sun, Z.; Jiang, B.; Xie, D.; Dawes, R.; Guo, H. Communication: Rigorous quantum dynamics of $O + O_2$ exchange reactions on an *ab initio* potential energy surface substantiate the negative temperature dependence of rate coefficients. *J. Chem. Phys.* **2014**, *141*, 081102.
- (39) Tyuterev, V. G.; Kochanov, R.; Campargue, A.; Kass, S.; Mondelain, D.; Barbe, A.; Starikova, E.; De Backer, M.; Szalay, P.; Tashkun, S. Does the “reef structure” at the ozone transition state towards the dissociation exist? New insight from calculations and ultrasensitive spectroscopy experiments. *Phys. Rev. Lett.* **2014**, *113*, 143002.

- (40) Hernandez-Lamonedada, R.; Salazar, M. R.; Pack, R. Does ozone have a barrier to dissociation and recombination? *Chem. Phys. Lett.* **2002**, *355*, 478–482.
- (41) Schinke, R.; Fleurat-Lessard, P. The transition-state region of the $O(^3P) + O_2(^3\Sigma_g^-)$ potential energy surface. *J. Chem. Phys.* **2004**, *121*, 5789–5793.
- (42) Holka, F.; Szalay, P. G.; Müller, T.; Tyuterev, V. G. Toward an improved ground state potential energy surface of ozone. *J. Phys. Chem. A* **2010**, *114*, 9927–9935.
- (43) Byron, S. R. Measurement of the Rate of Dissociation of Oxygen. *J. Chem. Phys.* **1959**, *30*, 1380–1392.
- (44) Shatalov, O. P. Molecular dissociation of oxygen in the absence of vibrational equilibrium. *Combust. Explos. Shock Waves* **1973**, *9*, 610–613.
- (45) Veliz, J. C. S. V.; Koner, D.; Schwilk, M.; Bemish, R. J.; Meuwly, M. The $C(^3P) + O_2(^3\Sigma_g^-) \leftrightarrow CO_2 \leftrightarrow CO(^1\Sigma^+) + O(^1D)/O(^3P)$ Reaction: Thermal and Vibrational Relaxation Rates from 15 K to 20000 K. *Phys. Chem. Chem. Phys.* **2021**, *23*, 11251–11263.
- (46) Guillon, G.; Honvault, P.; Kochanov, R. V.; Tyuterev, V. G. First-Principles Computed Rate Constant for the $O + O_2$ Isotopic Exchange Reaction Now Matches Experiment. *J. Phys. Chem. Lett.* **2018**, *9*, 1931–1936.
- (47) Qu, Z.-W.; Zhu, H.; Grebenshchikov, S. Y.; Schinke, R. The photodissociation of ozone in the Hartley band: A theoretical analysis. *J. Chem. Phys.* **2005**, *123*, 074305.
- (48) Nikitin, E. E. *Theory of Elementary Atomic and Molecular Processes in Gases*; Oxford University Press: Oxford, 1974.
- (49) Andrienko, D. A.; Boyd, I. D. Rovibrational energy transfer and dissociation in O_2-O collisions. *J. Chem. Phys.* **2016**, *144*.

- (50) Mankodi, T. K.; Bhandarkar, U. V.; Puranik, B. P. Dissociation cross sections for $\text{N}_2 + \text{N} \rightarrow 3\text{N}$ and $\text{O}_2 + \text{O} \rightarrow 3\text{O}$ using the QCT method. *J. Chem. Phys.* **2017**, *146*.
- (51) Zhang, T.; Lu, Y.; Cheng, X. State-Specific Dynamic Study of the Exchange and Dissociation Reaction for $\text{O}(^3\text{P})$ and $\text{O}_2(^3\Sigma_g^-)$ Collision by Quasi-Classical Trajectory. *Russ. J. Phys. Chem. A* **2022**, *96*, 876–883.